$^{10}B+^{13}C$ and $^{11}B+^{12}C$ reactions from 4 to 9 MeV/nucleon

J. F. Mateja
Physics Department, Tennessee Technological University, Cookeville, Tennessee 38505

A. D. Frawley
Physics Department, Florida State University, Tallahassee, Florida 32304

D. G. Kovar, D. Henderson, H. Ikezoe, R. V. F. Janssens, G. Rosner, G. S. F. Stephans, B. Wilkins, K. T. Lesko, and M. F. Vineyard
Argonne National Laboratory, Argonne, Illinois 60439

(Received 9 October 1984)

Reaction products arising from the interaction of $^{11}B+^{12}C$ and $^{10}B+^{13}C$ have been studied in the energy range $4<E_{lab}(B)<9$ MeV/nucleon. From the total fusion cross sections for the two entrance channels, the critical angular momenta have been extracted and then compared as a function of compound nucleus excitation energy. Even though a limitation in the fusion cross section was observed, no common limitation was found in the critical angular momenta for these two systems up to at least a ^{23}Na excitation energy of 60 MeV. Above this excitation energy, the experimental uncertainties make this point less clear. Up to an excitation energy of 60 MeV in ^{23}Na, a fusion limitation based on reaching a critical density of compound nucleus states like the yrast or "statistical" yrast line cannot be responsible for the fusion cross section limitations observed for these entrance channels. The present data suggest that competing entrance channel processes are responsible for the observed fusion cross section limitations.

I. INTRODUCTION

We have, over the last several years, studied four entrance channels which form the ^{23}Na compound nucleus[1–4] in an effort to understand the mechanism or mechanisms responsible for the limitations observed in fusion cross sections of light heavy-ion systems.[5–8] Over an energy region from approximately one to three times the Coulomb barrier (from 2 to 5 MeV/nucleon), our earlier studies appear to have ruled out a limitation mechanism based on a critical density of states in the compound nucleus.[7–9] Rather, these results suggested that competing entrance channel processes produce the observed fusion cross section limitations in that energy region.

The possibility still existed, however, that a critical density of compound nucleus states like the compound nucleus yrast or "statistical" yrast line might become important at higher bombarding energies. Such is the case in a recent study by DiGregorio *et al.*[10] of four entrance channels which form the ^{27}Al compound nucleus. In this study, it was found that for $E^*(^{27}Al)>60$ MeV the curves for E^* versus the critical angular momentum for each system converge, a condition which is indicative of a limitation imposed by the compound nucleus. With this in mind, an investigation was initiated which utilized the Argonne National Laboratory (ANL) tandem-linac accelerator to extend the energy range for two of the entrance channels studied at lower energies, the $^{11}B+^{12}C$ and the $^{10}B+^{13}C$ channels. The results of the Argonne work along with some of the results from our earlier work are presented here.

II. EXPERIMENTAL PROCEDURE AND ANALYSIS METHODS

The measurements were performed using beams of ^{10}B and ^{11}B obtained from the Argonne National Laboratory tandem-linac accelerator. Boron bombarding energies were chosen such that the ^{23}Na compound nucleus was formed at similar excitation energies [i.e., $E_x(^{23}Na)=49$, 60, and 70 MeV)] by the two entrance channels. The boron beams were incident on self-supporting ^{12}C and ^{13}C targets whose nominal thicknesses were 100 $\mu g/cm^2$.

The reaction products resulting from the target-projectile interactions were mass identified using a time-of-flight system which consisted of a microchannel plate and surface-barrier detector. A two-dimensional time versus energy spectrum was recorded on line. After making a time to mass conversion, a mass versus energy spectrum like that shown in Fig. 1 for the $^{11}B+^{12}C$ entrance

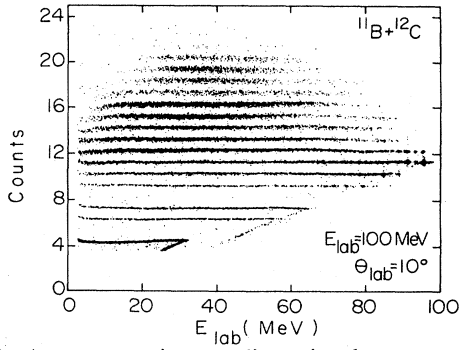

FIG. 1. A representative two-dimensional mass versus energy plot for the $^{11}B+^{12}C$ entrance channel.

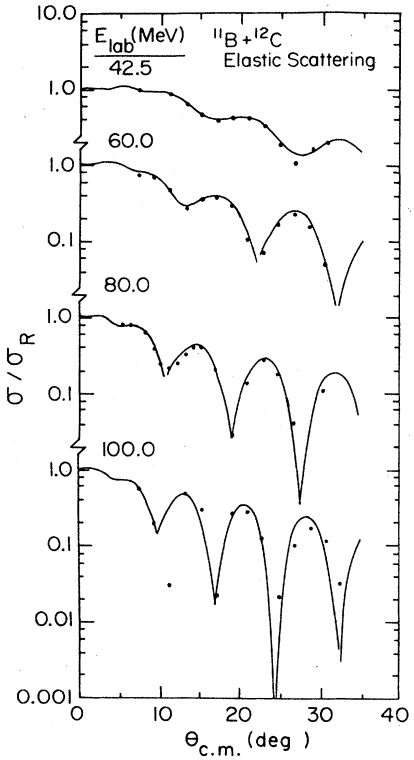

FIG. 2. The $^{11}B+^{12}C$ elastic scattering angular distributions. The optical model parameters were taken from Ref. 2. The angular distribution at 100 MeV was not used in determining the $^{11}B+^{13}C$ normalization constant.

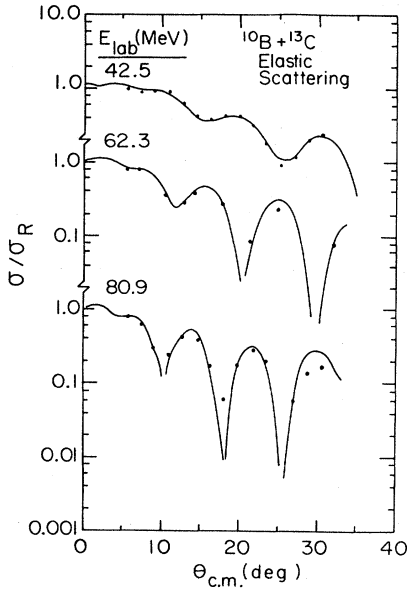

FIG. 3. The $^{10}B+^{13}C$ elastic scattering angular distributions. The optical model parameters were taken from Ref. 2. All three angular distributions were used in determining the $^{10}B+^{13}C$ normalization constant.

channel at 100 MeV was obtained. The turnover in the mass 4, 6, and 7 groups reflects the fact that the high energy particles in these reaction products were not completely stopped by the E detector. This effect only occurred for the mass 6 and 7 groups at our highest ^{11}B bombarding energy, 100 MeV. The high energy mass 4 particles were not fully stopped at any bombarding energy.

The efficiency of the time-of-flight system for any particle varies with the particle's mass and energy. The efficiency variation is due to the changing number of electrons produced in the channel-plate start detector. The efficiency of the time-of-flight detector was found experimentally by comparing the elastic yield in the singles energy spectrum with the corresponding elastic yield in the time spectrum. In addition to the ^{10}B and ^{11}B beams used in the fusion measurements, a ^{7}Li beam was used to determine the efficiency of the lighter masses. Corrections on the order of 25% were made to the Li data, while approximately 8% corrections were made to the B data. We expect the corrections to depend on energy as well as mass. As we have not measured the energy dependence of the efficiency correction in any great detail, we believe that the overall uncertainty in the preceding corrections is on the order of 5—10%. The efficiency corrections, of course, only apply to the lightest residue masses (≤ 11). Above this mass no channel plate efficiency correction is required.

Angular distributions for masses >4 were measured over the angular range $3° < \theta_{lab} < 35°$ in the $^{11}B+^{12}C$ experiment and $3° < \theta_{lab} < 40°$ in the $^{10}B+^{13}C$ study. The angular increments used in the two experiments varied from 0.5° at forward angles to 5° at backward angles. In addition to current integration, a monitor detector which recorded elastic scattering events was used to obtain a relative normalization for these data. The beam direction and consequently the time-of-flight detector angle were established to $<0.02°$ by making left-right measurements with the time-of-flight arm. To eliminate beam direction changes during the measurement of an angular distribution, beam refocusing was held to a minimum. To ensure that the beam direction did not change, the left-right measurements were repeated a number of times during each angular distribution.

Absolute cross sections for the two experiments were determined by comparing the elastic scattering yields, obtained simultaneously with the reaction residues, with optical model predictions (see Figs. 2 and 3). The optical model parameters which were used in this study, presented in Table I, were taken from Ref. 2. At our overlap en-

TABLE I. Optical model parameters for the elastic scattering of ^{11}B from ^{12}C and ^{10}B from ^{13}C.

System	V_0 (MeV)	r_r (fm)	a_r (fm)	W_0 (MeV)	r_i (fm)	a_i (fm)
$^{10}B+^{13}C$	66.85	1.094	0.609	10.00	1.200	0.700
$^{11}B+^{12}C$	60.50	1.094	0.609	36.04	1.182	0.487

ergy of 42.5 MeV, the total fusion cross section for the ANL $^{10}B+^{13}C$ study agreed to within 2% with the earlier Florida State results, while the agreement between the ANL and Florida State total fusion cross sections for the $^{11}B+^{12}C$ system was within 5%.

The uncertainties in the absolute values of the total fusion cross sections are attributable to counting statistics ($<2.5\%$), identification of fusion events in those mass groups containing nonfusion reaction products ($<3\%$), extrapolation of the data to zero degrees and beyond the largest angle measured in each experiment (2%), and errors associated with extracting the absolute cross section by normalizing the elastic scattering data with the optical model predictions (7%). The total uncertainty in the absolute cross sections is, therefore, approximately 8%.

In evaluating the total fusion cross section for any heavy-ion system, care must be taken to ensure the proper identification of fusion events. The energy spectra of all mass groups were inspected for evidence of nonfusion events, e.g., direct transfer, inelastic scattering, or projectile fragmentation, before that mass was included in the determination of the total fusion cross section. To assist in the identification of fusion events, the results of a Monte Carlo computer simulation of the successive evaporation of protons, neutrons, and alpha particles from an equilibrated but highly excited compound nucleus were compared with the data on a mass-by-mass basis. The computer code LILITA (Ref. 11) was used for these calculations.

For the $^{10}B+^{13}C$ entrance channel, the shapes and energy centroids of the calculated energy spectra for masses 13 to 22 were in good agreement with the experimental data. The results displayed in Figs. 4 and 5 for masses 15 and 20 were typical of masses in this range. As can be seen in these figures, the energy dependence of the data is well reproduced by the calculations at all bombarding energies. For masses 6—12, a substantial fraction of the yield lies well outside the energy range predicted by the fusion-evaporation calculation. Typical of masses 9—12 is mass 11 for which energy spectra are displayed in Fig. 6. Evident at high energies and forward angles are discrete states which are characteristic of direct transfer or inelastic scattering mechanisms. Consistent with this interpretation is the fact that this yield decreases rapidly with angle, a result which can be clearly seen when the forward and backward angle energy spectra in Fig. 6 are compared.

Also shown in Fig. 6 for the 8° and 16° mass 11 energy spectra are the fusion-evaporation predictions for this mass. The calculated fusion energy spectra have been used as a guide to determine the high energy fusion-evaporation cutoff for each mass. The upper limit was taken at the point where the calculated fusion-evaporation curve had fallen to 80—90% of the peak intensity. The remainder of the yield in a particular mass group was then attributed to nonfusion processes. In computing the fusion yield to all mass groups it was assumed that the fusion events resulted from the evaporation of only light

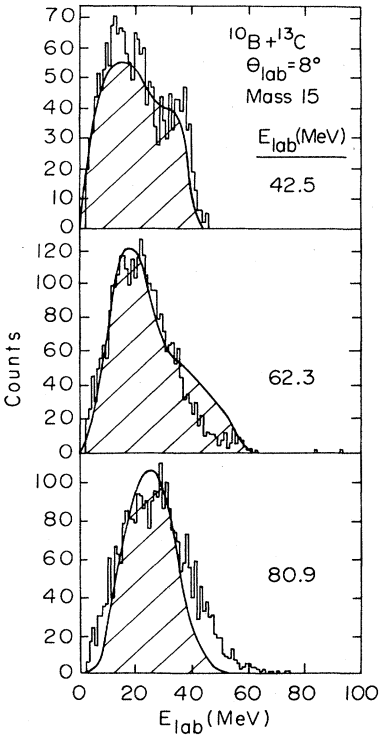

FIG. 4. The energy spectrum for the mass 15 residue resulting from the $^{10}B+^{13}C$ reaction. The histogram represents the data smoothed over 1 MeV energy intervals, while the dashed areas are the results from the Monte Carlo Hauser-Feshbach calculations.

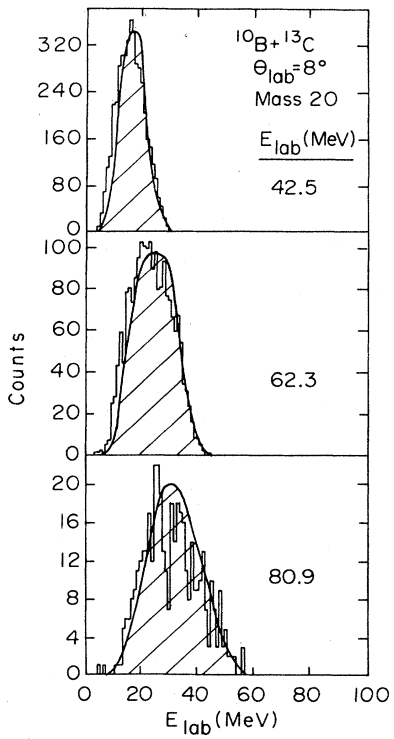

FIG. 5. The energy spectrum for the mass 20 residue resulting from the $^{10}B+^{13}C$ reaction. The histogram represents the data smoothed over 1 MeV energy intervals, while the dashed areas are the results of the Monte Carlo Hauser-Feshbach calculations.

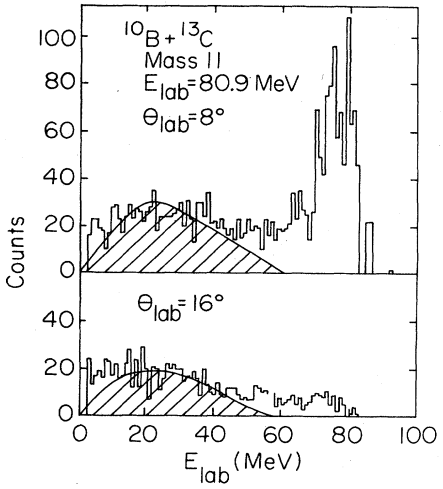

FIG. 6. The energy spectrum for the mass 11 residue resulting from the $^{10}B+^{13}C$ reaction at 80.9 MeV at 8° and 16°. The histogram represents the data smoothed over 1 MeV energy intervals, while the dashed areas are the results of the Monte Carlo Hauser-Feshbach calculation.

particles (i.e., p, d, t, ^{4}He, etc.); that is, there was no emission of heavy ions from the compound nucleus. If this assumption is not valid, then some double counting of fusion events has occurred. It is anticipated, however, that the cross section for the emission of heavy particles is not large and, therefore, the error introduced by this assumption is small.

The mass 6 and 7 groups displayed in Figs. 7 and 8, on the other hand, are dominated by a broad continuum peak. At 42.5 and 62.3 MeV, this peak is centered at an energy which corresponds to the beam velocity at all scattering angles. At 80.9 MeV, the velocity centroid of the continuum peak is near that of the beam at forward angles. At back angles, however, the continuum peak displays both a high and a low energy velocity component. The low energy component of the 80.9 MeV data is consistent with the fusion-evaporation calculations for masses 6 and 7. The energy centroids of the high energy components of the mass 6 and 7 spectra are reasonably well

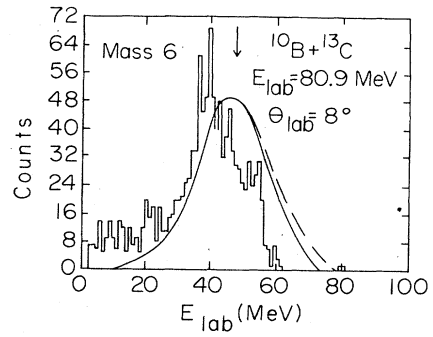

FIG. 7. The energy spectrum for the mass 6 residue resulting from the $^{10}B+^{13}C$ reaction at 80.9 MeV at 8°. The histogram represents the data smoothed over 1 MeV energy intervals. The solid curve is the result of a projectile breakup calculation which assumed that the system was left in a three-body final state after interaction, while the dashed curve is a calculation for a system left in a two-body final state.

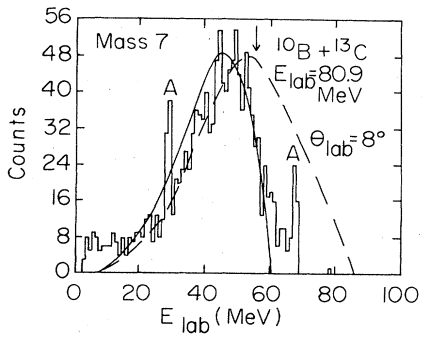

FIG. 8. The energy spectrum for the mass 7 residue resulting from the $^{10}B+^{13}C$ reaction at 80.9 MeV at 8°. The histogram represents the data smoothed over 1 MeV energy intervals. The solid curve is the result of a projectile breakup calculation which assumed that the system was left in a three-body final state after the interaction, while the dashed curve is for a system left in a two-body final state. The two peaks labeled with an "*A*" in the figure arise from the ^{1}H(^{10}B, ^{7}Be)^{4}He reaction.

predicted by the simplest of projectile breakup models. In such calculations, it is assumed that the detected particle is merely a spectator whose velocity is unaltered during the interaction. A particle of mass "*m*" would therefore be emitted in the $^{10}B+^{13}C$ reaction with an energy $m/10$ times the energy of the elastically scattered particle. These energies have been identified with arrows in Figs. 7 and 8.

A more realistic model has also been used to describe the breakup process.[3,12,13] In this model the final momentum of the detected fragment is determined by both the velocity of the projectile and the intrinsic momentum of the fragment relative to the remainder of the projectile. Two breakup reaction mechanisms have been considered. In the first, it was assumed that after the breakup of the projectile one of the fragments was captured by the target nucleus (a process which is commonly known as direct transfer to the continuum). As can be seen in Fig. 9(a),

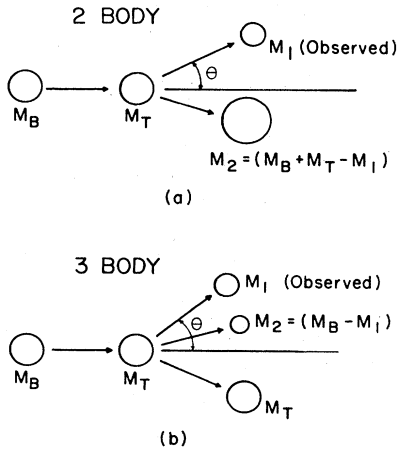

FIG. 9. (a) Schematic representation of projectile breakup followed by capture of one of the fragments. (b) Schematic representation of breakup with both breakup particles remaining free after the interaction. The reactions represented in (a) and (b) result in two- and three-body final states, respectively.

this mechanism results in a two-body final state. The other reaction process assumes that neither fragment is captured after breakup. This process, leaving three bodies in the final state, is depicted in Fig. 9(b). A complete description of the calculations is presented in Ref. 3.

For the $^{10}B+^{13}C$ mass 6 and 7 groups, the results of the calculations are compared with the data in Figs. 7 and 8, respectively. For this comparison it has been assumed that the primary breakup channels for the mass 6 and 7 groups are ^{6}Li and ^{7}Li. This is probably a reasonable assumption for the mass 6 exit channel as the breakup energy for ^{10}B going to either $^{6}He+^{4}Li$ or $^{6}Be+^{4}H$ exit channels is much larger than that for $^{6}Li+^{4}He$. The assumption that the mass 7 group is primarily due to ^{7}Li is probably not valid since the ^{10}B breakup energies to the $^{7}Li+^{3}He$ and $^{7}Be+^{3}H$ are approximately equal. However, one finds that the predictions by the breakup calculation for $^{7}Li+^{3}He$ and $^{7}Be+^{3}H$ are similar.

In Figs. 7 and 8, the energy distribution which arises when the system is left in a two-body final state is represented by the dashed curve, while the energy distribution for a system left in a three-body final state is represented by the solid curve. One result of the calculation which might be noted is the difference in the calculated two- and three-body energy centroids which appears in the ^{7}Li exit channel but not in the ^{6}Li. The centroid shift in the ^{7}Li case is primarily due to a large difference between the two- and three-body reaction Q values (23 MeV). The Q-value difference in the ^{6}Li channel is considerably smaller, 6.4 MeV, and the centroid shift is consequently smaller. While the overall agreement between the calculations and the data is reasonably good, there is no sufficient difference in the two- and three-body results to unambiguously choose one over the other. However, the results do, we believe, support the contention that this yield arises from the breakup of the ^{10}B projectile.

Results similar to those described previously were obtained in the $^{11}B+^{12}C$ experiment. In this work, the yield in masses 14 to 22 is in good agreement with the fusion-evaporation calculations. The mass groups within one or two mass units of either the target or projectile mass (masses 9—13) display strong discrete states whose strengths decrease rapidly with angle. Again these are characteristics of direct transfer, inelastic scattering, or knockout reaction mechanisms. For masses 6 and 7, the spectra are again dominated by a broad continuum peak. While reasonable agreement between the data and the breakup model calculations is found for these two mass groups, a low energy component is also apparent. The low energy component is consistent with the fusion-evaporation calculations.

III. EXPERIMENTAL RESULTS AND DISCUSSION

Excitation functions for the fusion-evaporation products from the $^{11}B+^{12}C$ and $^{10}B+^{13}C$ reactions are presented in Figs. 10 and 11. In Figs. 12 and 13 the total

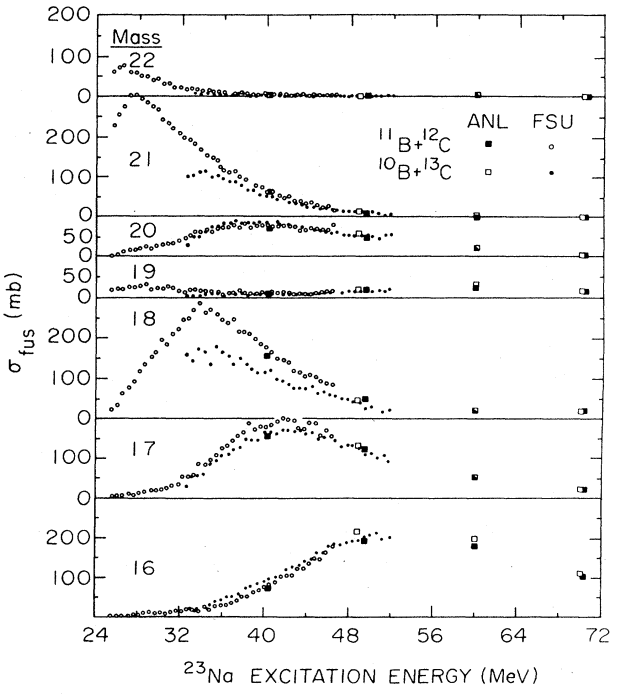

FIG. 10. Angle-integrated cross sections of fusion-evaporation residues for masses 16—22 from the $^{11}B+^{12}C$ and $^{10}B+^{13}C$ reactions. Uncertainties in the elemental cross sections are approximately 8% for masses 16—22.

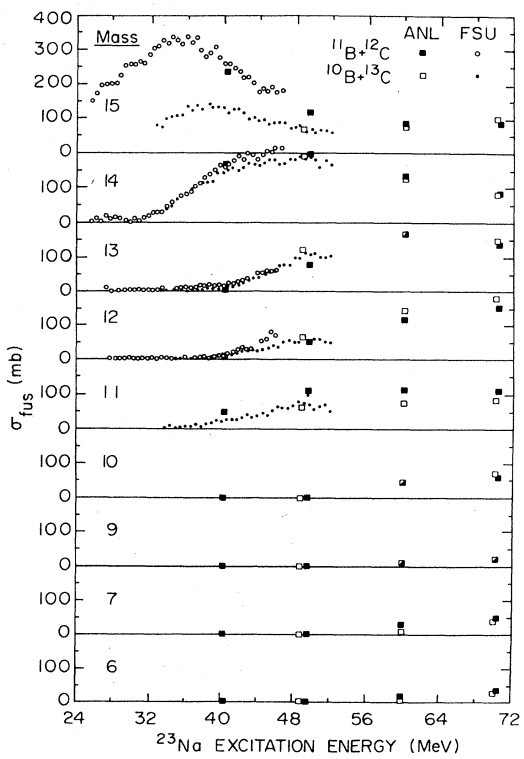

FIG. 11. Angle-integrated cross sections of fusion-evaporation residues for masses 6—15 from the $^{11}B+^{12}C$ and $^{10}B+^{13}C$ reactions. Uncertainties of the elemental cross sections are approximately 8% for the strong groups dominated by fusion. For masses 6—12, where a nonfusion contribution is present and there is an efficiency correction for the channel plate, the uncertainties can be as large as 25%.

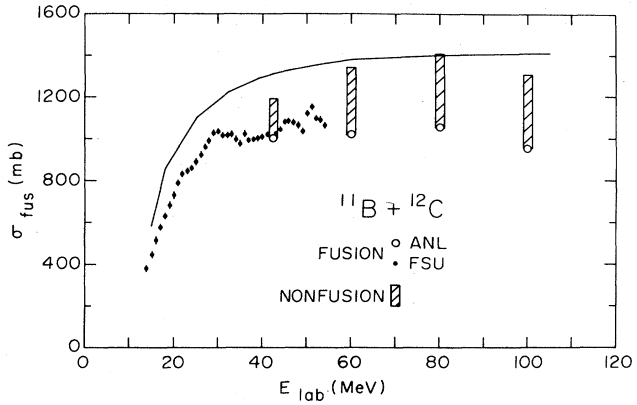

FIG. 12. The total fusion cross section for the $^{11}B+^{12}C$ entrance channel as a function of E_{lab}.

fusion cross sections for these systems are displayed. Also presented in Figs. 12 and 13 (solid curves) are the total reaction cross sections obtained from the optical model analyses. As can readily be seen, the trend which began at low energies, a gradual separation of the total reaction and fusion cross sections, continues at the higher bombarding energies. Limitations like these in fusion cross sections have been discussed by a number of authors.[5–10]

The total fusion cross sections measured in the ANL work (see Table II) have been used to extract the critical angular momenta for the two systems according to the usual sharp-cutoff approximation:

$$\sigma_{\text{fus}}=\pi\lambda^2\sum_{l=0}^{l_{\text{cr}}}(2l+1)\ .$$

If the limitation in the fusion cross section is brought about by reaching a critical density of compound nucleus states like the yrast or the "statistical" yrast line,[7–9] then a plot of the critical angular momenta as a function of compound nucleus excitation energy should display a common limitation in the energy region where the fusion cross section limitation occurs. As can be seen in Fig. 14, no common limitation is found in the critical angular momenta for the $^{11}B+^{12}C$ and $^{10}B+^{13}C$ entrance channels below an energy of at least 60 MeV in the ^{23}Na compound nucleus. This, despite the fact that the fusion cross sections for these two entrance channels are clearly being limited below this energy (see Figs. 12 and 13). This rules out a fusion limitation process based solely on reaching a critical density of compound nucleus states in this energy region. At our highest bombarding energy the experimental uncertainty prevents us from drawing a conclusion either way.

TABLE II. The total fusion cross sections measured in the ANL experiment for the $^{11}B+^{12}C$ and $^{10}B+^{13}C$ reactions.

System	Laboratory energy (MeV)	Fusion cross section (mb)
$^{11}B+^{12}C$	42.5	1005
	60.0	1021
	80.0	1051
	100.0	951
$^{10}B+^{13}C$	42.5	971
	62.3	1004
	80.9	1005

That the limitation in the fusion cross section is brought about by competing entrance channel processes for ^{23}Na excitation energies <60 MeV can be seen if one considers the nonfusion cross sections measured in the present experiment. The nonfusion component of each mass group is tabulated in Table III and displayed for the two entrance channels in Figs. 15 and 16. The total nonfusion strength along with the fusion and total reaction cross sections for the $^{11}B+^{12}C$ and $^{10}B+^{13}C$ reactions at

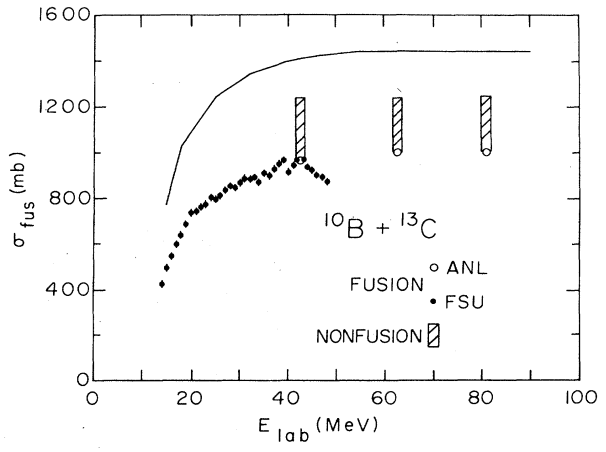

FIG. 13. The total fusion cross section for the $^{10}B+^{13}C$ entrance channel as a function of E_{lab}. It should be noted that within the experimental uncertainties of the data and the calculated total reaction cross section, the combined fusion and nonfusion strength measured in the present experiment is in agreement with the calculated total reaction cross section.

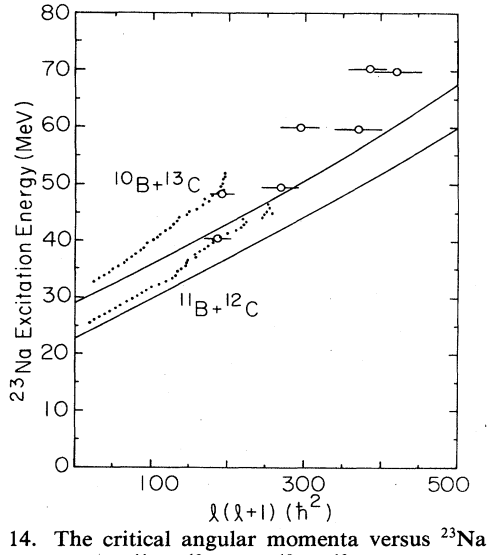

FIG. 14. The critical angular momenta versus ^{23}Na excitation energy for the $^{11}B+^{12}C$ and $^{10}B+^{13}C$ entrance channels. The grazing angular momenta (solid lines) were obtained from the optical model parameters listed in Table I.

TABLE III. Nonfusion cross sections for masses 6–13. The estimated uncertainties in the nonfusion cross sections are approximately 8% for the strong groups and can be as large as 25% for the weaker groups due to uncertainties in separating fusion and nonfusion yields.

		Nonfusion cross section (mb)						
	Energy	Mass						
System	(MeV)	6	7	9	10	11	12	13
$^{11}B+^{12}C$	100.0	20	35	22	72	127	64	14
	80.0	18	38	17	54	147	69	12
	60.0	18	37	12	48	140	47	16
	42.5	8	12	4	16	94	41	10
$^{10}B+^{13}C$	80.9	45	39	45	67	34	11	2
	62.3	48	47	22	79	34	4	1
	42.5	21	28	18	135	61	2	

the various energies studied are presented in Table IV and displayed in Figs. 12 and 13. In the $^{11}B+^{12}C$ study, the combined fusion and nonfusion strength accounts for 91% to 101% of the total reaction cross section. In the $^{10}B+^{12}C$ work, the combined strength ranges from 87% to 88% of the total reaction cross section. Thus, the nonfusion cross sections observed in the present experiment account for most of the missing reaction strength. The remaining few percent of the missing total reaction strength, if indeed real, may be in reaction processes which produce only very light particles (p, d, t, ^{3}He, and ^{4}He), particles not studied in the present experiment. That a substantial part of the cross section might go into reaction channels which produce only light particles has also been suggested in an earlier study at $E_{lab}(B)=54$ MeV of the light particles emitted in these two reactions.[3]

Finally, two additional features of the data might be noted. First, a comparison of the total fusion cross sections for the two entrance channels (see Figs. 12 and 13 and Table IV) reveals that both systems reach maximum fusion cross sections of approximately 1000 mb. Similar results, maximum fusion cross sections from approximately 900 to 1000 mb, have been obtained for a number of entrance channels in this mass region.[5] What these systems have in common is that both interacting ions have valence nucleons occupying only the $1p$ shell. Other systems in this mass region, however, with valence nucleons in the $1s$-$2d$ shells have maximum fusion cross sections of approximately 1200 mb.[5] This particular feature of the data is still not completely understood.

The second interesting feature of the present data is concerned with the individual residue cross sections. As can be seen in Figs. 10 and 11, the residue cross sections, when compared at the same ^{23}Na excitation energy, are entrance channel independent at the energies measured in the ANL experiment (i.e., the cross section for a given residue mass is the same for the $^{11}B+^{12}C$ and the $^{10}B+^{13}C$ reactions at the same ^{23}Na excitation energy). The cross section differences which occurred in the different mass groups at lower energies, for example in mass 15, have completely disappeared at the higher bombarding energies. The differences in mass distributions between $^{11}B+^{12}C$ and $^{10}B+^{13}C$ at the lower bombarding energies could be qualitatively explained in terms of the angular momenta brought into the compound nucleus by the two entrance channels and differences in the limited number of decay channels which were capable of carrying away high angular momenta.[2] However as the energy increases, the number of decay channels capable of removing high angular momenta from the compound nucleus increases rapidly, while the grazing angular momentum in the entrance channel increases relatively slowly (see Fig. 14). Apparently, at the highest energies reached in this work, the differences in the number of decay channels capable of carrying away large angular momenta are no longer important. The preceding arguments, of course, assume that the reaction processes which compete with fusion for entrance channel flux do not have substantially different angular momentum dependences for the $^{11}B+^{12}C$ and $^{10}B+^{13}C$ entrance channels.

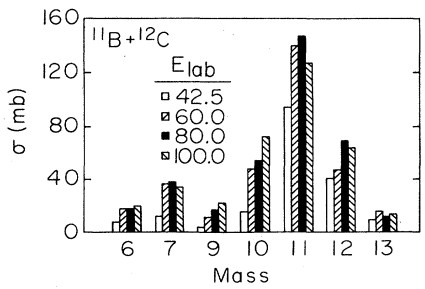

FIG. 15. Total nonfusion cross sections observed in the $^{11}B+^{12}C$ reaction.

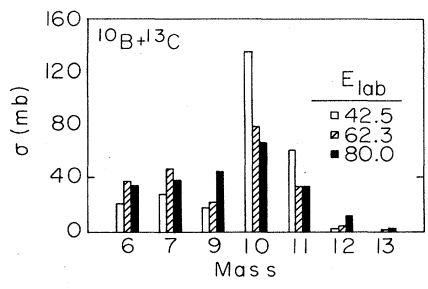

FIG. 16. Total nonfusion cross section in the $^{10}B+^{13}C$ reaction.

TABLE IV. The total fusion, nonfusion, and reaction cross sections for the $^{11}B+^{12}C$ and $^{10}B+^{13}C$ entrance channels.

System laboratory energy (MeV)	Fusion cross section (mb)	Nonfusion cross section (mb)	Combined fusion + nonfusion cross section (mb)	Total[a] reaction cross section (mb)
$^{11}B+^{12}C$				
42.5	1005	185	1190	1311
60.0	1021	318	1339	1374
80.0	1051	355	1406	1399
100.0	951	354	1305	1405
$^{10}B+^{13}C$				
42.5	971	265	1236	1410
62.3	1004	235	1239	1446
80.9	1005	243	1248	1444

[a]Obtained using the optical model parameters listed in Table I.

IV. SUMMARY

In studying the fusion-evaporation cross sections for the $^{11}B+^{12}C$ and $^{10}B+^{13}C$ reactions, the fusion cross section limitations for these entrance channels appear to occur because of competition for entrance channel flux between fusion and other entrance channel reaction processes up to an excitation energy of at least 60 MeV in the ^{23}Na compound nucleus. Only at our highest bombarding energy [$E_x(^{23}Na)=70$ MeV] is there a possibility that a limitation might occur because a critical density of states in the compound nucleus like the yrast or "statistical" yrast line has been reached.

[1]J. F. Mateja, A. D. Frawley, L. C. Dennis, K. Abdo, and K. W. Kemper, Phys. Rev. Lett. **47**, 311 (1981).
[2]J. F. Mateja, A. D. Frawley, L. C. Dennis, K. Abdo, and K. W. Kemper, Phys. Rev. C **25**, 2963 (1982).
[3]J. F. Mateja, J. Garman, and A. D. Frawley, Phys. Rev. C **28**, 1579 (1983).
[4]J. F. Mateja, J. Garman, D. E. Fields, R. L. Kozub, A. D. Frawley, and L. C. Dennis, Phys. Rev. C **30**, 134 (1984).
[5]D. G. Kovar, D. F. Geesaman, T. H. Braid, Y. Eisen, W. Henning, T. R. Ophel, M. Paul, K. E. Rehm, S. J. Sanders, P. Sperr, J. P. Schiffer, S. L. Tabor, S. Vigdor, and B. Zeidman, Phys. Rev. C **20**, 1305 (1979), and references therein.
[6]J. Gomez del Campo, R. G. Stokstad, J. A. Biggerstaff, R. A. Dayras, A. H. Snell, and P. H. Stelson, Phys. Rev. C **19**, 2170 (1979).
[7]J. P. Wieleczko, S. Harar, M. Conjeaud, and F. Saint-Laurent, Phys. Lett. **93B**, 35 (1980).
[8]F. Saint-Laurent, M. Conjeaud, and S. Harar, Nucl. Phys. **A327**, 517 (1979).
[9]S. M. Lee, T. Matsuse, and A. Arima, Phys. Rev. Lett. **45**, 165 (1980).
[10]D. E. DiGregorio, J. Gomez del Campo, Y. D. Chan, J. L. C. Ford, Jr., and D. Shapira, Phys. Rev. C **26**, 1490 (1982).
[11]J. Gomez del Campo and R. G. Stokstad, Oak Ridge National Laboratory, Report No. ORNL/TM-7295, 1981.
[12]R. Serber, Phys. Rev. **72**, 1008 (1947).
[13]N. Matsuoka, A. Shimizu, K. Hosono, T. Saito, M. Kondo, H. Sakaguchi, Y. Toba, A. Goto, F. Ohtani, and N. Nakanishi, Nucl. Phys. **A311**, 173 (1978).